Fabrication of a stable light-activated and p/n type AgVO3/V2O5-TiO2 heterojunction for pollutants removal and photoelectrochemical water splitting

Hai Yu (yuhai19910806@163.com)
Anhui University
Zhang Miao
Anhui University
Yanfen Wang
Anhui University
Jianguo Lv
Hefei Normal University
Lei Yang
Hefei University
Yanmei Liu
Anhui University
Qian Gao
Anhui University
Gang He
Anhui University
Zhaoqi Sun
Anhui University

Research Article

Keywords: Double type-II band gap, Fermi level alignment, P-n junction heterojunction, Donor density, Photoelectrochemical activity

Posted Date: July 24th, 2021

DOI: https://doi.org/10.21203/rs.3.rs-736841/v1

Version of Record: A version of this preprint was published at Journal of Alloys and Compounds on October 1st, 2021. See the published version at https://doi.org/10.1016/j.jallcom.2021.162500.

Abstract

In this study, TiO_2 nanorod arrays (TiO_2) was fabricated and modified with the $AgVO_3$ quantum dots (QDs) decorate on interfacing few-layer V_2O_5 to form a heterojunction material for removal pollutants and photoelectrochemical (PCE) water splitting. The $AgVO_3/V_2O_5$-TiO_2 nanorod arrays ($AgVO_3/V_2O_5$-TiO_2) synthesized by the secondary hydrothermal method were loaded with conductive glass, which facilitated the formation of one-dimensional (1D) nanorod and p-n junction structures. Through instrumentations, to investigate the structural, morphological, optical, photocatalytic and PCE characteristics of the materials. The TiO_2 modified by $AgVO_3$ and V_2O_5 can significantly improve the visible light optical absorption, the reduce the electron-hole pair binding rate and shorten the band gap (3.07-1.41eV) of TiO_2. The resulting photocurrent density (116uA/cm^2) and photodegradation efficiency (rate constant, k = 0.025min^{-1}) of $AgVO_3/V_2O_5$-TiO_2 are approximately 20 (6uA/cm^2) and 5 times (0.005min^{-1}) higher than those of bare TiO_2, respectively. The $AgVO_3/V_2O_5$-TiO_2 achieved a current density of 10mA at an overpotential of 246.2mV and exhibited excellent oxygen evolution reaction (OER) performance. The systematic PEC experiments concluded that the optimized of the TiO_2 interface by $AgVO_3$ and V_2O_5 could promote the separation and transport of charge carriers.

1. Introduction

With the massive extraction of fossil fuels and their limited storage, solar energy has become the dominant option for future energy. Photoelectrochemical (PEC) water splitting technology uses two of the most abundant resources on earth - sunlight and water to produce sustainable and clean fuels. One of the main options for artificially achieving solar to chemical energy conversion is to integrate semiconductor materials with electrocatalysts in photovoltaic electrodes. Photovoltaic conversion converting solar energy to chemical energy is a prominent form of energy conversion. Photoconversion for solar-driven reactions shows wide promise in addressing energy and environmental challenges. However, a typical challenge in this field is that highly efficient photoabsorbers are not durable, while durable materials show poor efficiency. Therefore, the development of efficient and durable photovoltaic poles is crucial for solar energy production fuel applications. The performance of PEC and photocatalysis is largely dependent on the design of the photocatalyst. Properly tailored photocatalysts can achieve efficient light harvesting, excellent stability, facilitate charge separation and transport, and accelerate surface reactions [1]. In recent years, one-dimensional (1D) nanorod, nanotube and nanowire arrays have received increasing attention as photoelectrodes in PEC cell. The advantages of 1D nanostructured arrays are large surface area, fast electron transport paths, and low complexation rates [2, 3]. For instance, 1D undoped TiO_2 nanorod arrays with a length of 2.1um were synthesized by our group [4, 5]. It can absorb light at wavelengths below about 400nm in the simulated sunlight spectrum. In principle, a well-separated and aligned TiO_2 nanorod arrays is considered as an ideal light-harvesting device. This is due to the photogenerated holes (h^+) and electrons (e^-) inside the nanorods, which easily diffuse along the nanorod radius toward the side surface and the nanorod length toward the conductive glass substrate, thus

effectively inhibiting the recombination process of charge carriers. Since the realization of photocatalytic water splitting on TiO_2 electrode, semiconductor-based photocatalysis and photoelectrochemical water splitting has attracted tremendous attention. Specially, the bandgap of the TiO_2 rutile phase (~ 3.0eV) is lower than that of the TiO_2 anatase phase (~ 3.2eV), and the rutile phase is easy to prepare [4]. Therefore, the 1D TiO_2 nanorod arrays has great potential for applications in photodegradation, PEC cells and dye-sensitised solar cells.

The wide absorption spectrum, efficient charge transfer and good stability of the semiconductors are decisive factors for the degradation of water pollution and water splitting. In order to the absorption limit under the sunlight irradiation, various strategies have been proposed to improve the photocatalysis and PCE performance of TiO_2 materials, including nanostructures, passivated surfaces, co-catalysts, and doping with exotic elements. In general, most researchers develop composite materials using p-type materials and n-type photocatalysts, inspired by the basic p-n junction principle used in silicon solar cells [6, 7]. This structure is an excellent way to improve the light conversion efficiency of hybrid photocatalysts. TiO_2 photocatalyst is a common n-type semiconductor structure. For example, Kin. et al. reported that a TiO_2-MoS_2[8, 9], TiO_2-CuO and TiO_2-CuO/Cu_2O [10], composite photocatalyst exhibited better photocatalytic activity than bare TiO_2. On the other hand, a good conductive 1D in a heterostructured array system should have a synergistic result between the internal array and the external shell. The internal array is mainly responsible for the high conductivity and the outer shell acts as a light collector to increase the absorption of visible light. However, studies on 1D TiO_2 as an array of such composite structures are still lacking, which hinders further applications of 1D TiO_2 in photocatalysis and photoelectrochemical [11].

Recently, vanadium oxides (V_2O_5) have been studied because of their low-cost and environmental friendliness compared to metallic oxide. V_2O_5 is the most commonly used major p-type metal oxide catalyst because it is a rising photocatalyst due to its narrow bandgap(~ 2.2eV), abundance, low cost, and high stability [12–15]. The rutile phase TiO_2 nanorods is employed as a support due to their large surface area and high stability. $AgVO_3$ based nanostructures have been demonstrated to be excellent oxygen evolution reaction catalysts [16–20], including compatible semiconductor photocatalysts. $AgVO_3$ is used as an active additive and structure promoter to improve the catalyst activity of TiO_2. On the other hand, the Ag particles in $AgVO_3$ are photo-deposited between V_2O_5 and TiO_2 as an intermediate electron-conducting bridge. The surface of TiO_2 nanorods array increases the absorption of visible light through surface plasmon resonance. An ideal photocatalytic must be visible-light responsive, efficiently electron-hole separation and interfacial charge transfer, photochemically stable, as well as catalytic redox reaction[21].

Herein, we used 1D TiO_2 nanorods arrays, as the electron acceptor to promote charge delivery V_2O_5 and $AgVO_3$, as the photo-absorbers, to form p-n junction and Z heterostructure photoelectrode. The preparation process of $AgVO_3$/V_2O_5-TiO_2 is shown in Scheme 1. The inner array and the outer shell of

these heterostructured arrays are composed of TiO_2 and V_2O_5, respectively. $AgVO_3$ quantum dots were deposited on V_2O_5 surface by low temperature hydrothermal method. The contact between the three different energy levels of the semiconductors $AgVO_3$, V_2O_5 and TiO_2 involves charge redistribution, leading to the final formation of the synthesized semiconductor in a z-type heterojunction structure. Here, we present new heterostructure for amplifying the photocatalytic and photoelectrochemical (PEC) properties of $AgVO_3/V_2O_5$-TiO_2.

2. Experimental Section

2.1. Materials

All chemicals used in the this work are of analytical reagent grade, commercially available and were used as received without further purification. Tetrabutyl titanate ($C_{16}H_{36}O_4Ti$), hydrochloric acid (HCl-10mol per liter), silver nitrate ($AgNO_3$), ammonium metavanadate (NH_4VO_3) and ethyl alcohol (C_2H_6O) were purchased from Aladdin official online store. All aqueous solutions were prepared using deionized water (DW). The $AgVO_3/V_2O_5$-TiO_2 was prepared using a two-step hydrothermal method.

2.2. Preparation of hydrothermal $AgVO_3/V_2O_5$-TiO_2 photocatalysts

The TiO_2 nanorod arrays (TRA) were fabricated by a simple hydrothermal approach. In detail, 15mL of HCl, 15mL of DW and 0.5mL of $C_{16}H_{36}O_4Ti$ were mixed in a 50 mL beaker, stirring the mixture for 30 minutes before transferring to a Teflon lined autoclave (50mL). Pre-cleaned conductive glass (FTO) was used as a substratee ($1.5\times3cm^2$), and the mixture was transferred into a 50mL Teflon-lined autoclave, and the treatment was carried out at 150°C for 12h [4]. Finally, the obtained TRA was then collected and dried at 70°C overnight.

The V_2O_5-TiO_2 photocatalysts was also prepared by a similar strategy hydrothermal, as follows: 0.488g NH_4VO_3 was dissolved in a solution containing ethanol and DW (1:1) under a strong magnetic stirring for 60 min. Then, the pH of the solution was adjusted to 2.0 by adding HCl solution (1.0mol/L), with the solution color changing from milky white to orange [22].

The $AgVO_3/TiO_2$ materials were prepared by in hydrothermal method as follows: 0.5mmol NH_4VO_3 (about 0.12g) and 0.5mmol $AgNO_3$ (about 0.17g) were dissolved in 30mL DL under magnetic stirring (stirred for 2h) to obtain solution. Then, the aqueous solution and TiO_2 put into a 50mL Teflon-lined autoclave, and followed by treatment at 160°C for 6h. The synthesis $AgVO_3/V_2O_5$-TiO_2 process is shown in Scheme 1.

2.3. Characterization

The samples were characterized using various analytical methods. X-ray polycrystalline diffractometer (XRD, 9kW/SmartLab 9KW, Japan) measurement were made with monochromatic CuKa radiation in the range from 25° to 75°. The morphological and structural information of samples was characterized by field emission scanning electron microscopy (SEM, Hitachi-S4800, Dallas, TX, USA), high-resolution transmission electron microscopy (TEM, HITACHI, Tokyo, Japan), Energy dispersive X-ray spectroscopy (EDX), UV–visible spectrophotometry (Neosys-2000, SCINCO), photoluminescence (PL) spectroscopy (Perkin Elmer) and X-ray Photoelectron Spectrometer (XPS ESCALAB 250Xi/ESCALAB 250Xi, America).

2.4. Photocatalytic test

The photocatalytic ability of the as-synthesized samples were estimated by the measurement of the photo-degradation of methylene blue (MB) aqueous solution (20mg/L) under 150W simulated solar irradiation. The experiment was performed as follows: the samples with an area size of 1×1cm^2 were dispersed in a colorimetric reactor containing 5mL of MB solution. After in dark for 30min, approximately 3mL of the suspension was extracted at the given time interval and the typical absorption peak at 665nm was tracked with a UV-Vis spectrophotometer to evaluate the concentration of MB [4].

These rely on photo-excited charge carrier separation to achieve photocatalysis without any external photovoltaic or electrical equipment.

2.5. Photoelectrochemical (PCE) measurements

The photochemical measurements (CHI 660D, Chenhua, Shanghai) were performed at room temperature by an electrochemical workstation in a typical three electrode configuration. The reference electrode and counter electrode are a saturated Ag/AgCl electrode and a Pt wire. The working electrode is a sample with an exposed area of 1cm^2 and the electrolyte is an aqueous solution of 0.2M Na_2SO_3 and 0.1M Na_2S. The light source is a 150W xenon lamp used as a standard analogue illumination (AM 1.5G, 100mW/cm^2). The electrode potentials were converted to values versus a reversible hydrogen electrode (RHE) by using the Nernst equation:

$$V_{RHE}=E_{Ag/AgCl}+0.059pH+V^0_{Ag/AgCl},$$

where $E_{Ag/AgCl}$ is the experimental potential measured at the control Ag/AgCl reference electrode, and $V^0_{Ag/AgCl}$ is the standard potential of Ag/AgCl (0.198 V). Linear sweep voltammograms (LSV) were recorded at a scan rate of 10mV s^{-1} from negative to positive at pH = 13 in 0.2M Na_2SO_3 and 0.1M Na_2S electrolyte. More kinetics assessment was employed by EIS measurement, the frequency range was from 0.1Hz to 10kHz. Mott–Schottky measurements were performed at frequencies of 1000Hz with an amplitude of 0.01V in 0.2M Na_2SO_3 and 0.1M Na_2S aqueous solution at pH = 13.

3. Results And Discussion

3.1. Microstructure characterization and composition analysis

XRD analysis was performed to investigate the crystal structures of the samples. Figure 1 shows the XRD diffraction patterns of the samples, all diffractograms show similar peaks. The signals at 2θ = 36.0°, 41.2°, 54.3° and 62.7° characterize the of TiO_2, and two additional peaks at 2θ = 30.5° and 32.1° appear with related V_2O_5 and $AgVO_3$, respectively. The $AgVO_3/V_2O_5$-TiO_2 composite showed a compound of rutile TiO_2 phase (JCPDS 21-1276), V_2O_5 phase (JCPDS No.41-1426) [14]and $AgVO_3$ phase (JCPDS No.29-1154) [19], revealing that the mixture was the main composition of TiO_2, V_2O_5, $AgVO_3$ crystal structure. The absence of particularly strong signals from V_2O_5 indicates the V_2O_5 highly dispersed. All characteristic peaks of $AgVO_3$, V_2O_5 and TiO_2 are observed in the XRD pattern of $AgVO_3/V_2O_5$-TiO_2.

The photographs of TiO_2 and $AgVO_3/V_2O_5$-TiO_2 were exhibited in Fig. 2. During hydrothermal process, TiO_2 forms nanorod arrays at FTO, as shown in Fig. 2(a) and (b). For comparison, Fig. 2(c), d display SEM images of the $AgVO_3/V_2O_5$-TiO_2 in preparation.There is no essential change in morphology, but significantly increased surface roughness in comparison with bare TiO_2 precursor, which can be seen $AgVO_3$, V_2O_5 its completely covered on the TiO_2 nanorods surface. The diameter of these nanorods is 20-30nm under high magnification SEM observation.

In order to further investigate the microstructure and chemical composition distribution, TEM images and EDS elemental maps were tested in Fig. 3. Figure 3e represents the TEM images of $AgVO_3/V_2O_5$-TiO_2 and the corresponding EDS elemental profiles of Ti, O, V, and Ag, which exhibit the growth of V_2O_5 around the TiO_2 nanorods and the attachment of $AgVO_3$ to the outermost layer of the nanorods in the form of quantum dots ($AgVO_3$ QDs structure presents discrete distribution in V_2O_5-TiO_2 nanorod), confirming the successful formation of $AgVO_3/V_2O_5$-TiO_2 heterostructures. Figure 3a shows the TEM image of $AgVO_3/V_2O_5$-TiO_2 nanorod, an ultrathin coating layer with a thickness of about 10nm can be observed on the surface of TiO_2 nanorod and and its surface is roughly covered with a large number of small particles (can be identified as $AgVO_3$ QD), indicating the successful clad on TiO_2 rods to form a shell structure as V_2O_5-TiO_2, and $AgVO_3$ QD dispersed separately on the surface of V_2O_5-TiO_2, in good match with the elemental mapping images (Fig. 3e). Three HRTEM images gave further direct evidence for the formation of $AgVO_3/V_2O_5$-TiO_2, Fig. (3b, c and d) show an enlarged view of a partial area the $AgVO_3/V_2O_5$-TiO_2 in Fig. 2a, which can roughly distinguish TiO_2 nanorod, V_2O_5 thin film layers, and $AgVO_3$ QDs. The High-resolution TEM (HRTEM) images show different lattice fringes, lattice spacings of ~ 0.25nm correspond to the (101) crystal plane of rutile TiO_2, and the lattice spacing of ~ 0.37nm in the middle V_2O_5 layer corresponds to their (001) crystal plane, and the (501) lattice spacing of the outermost $AgVO_3$ QDs is 0.306 nm. It can be concluded that $AgVO_3$ QDs has been successfully attached to the surface of V_2O_5-TiO_2 nanoarray. All these findings well indicate that the $AgVO_3/V_2O_5$-TiO_2 nanoarrays were successfully synthesized on FTO substrates.

To further clarify the successful deposition of $AgVO_3$ and V_2O_5, X-ray photoelec-tron spectroscopy (XPS) was performed to characterize the surface chemical states of $AgVO_3/V_2O_5$-TiO_2. Figure 4a shows the survey XPS spectra results in line with the constituents. The distinct peaks of Ti, O, V, C, and Ag elements for $AgVO_3/V_2O_5$-TiO_2 and the peaks of Ti, C and O elements for TiO_2 can be found. Altogether, these observations indicate that TiO_2 nanorods are modified by V_2O_5 and $AgVO_3$ sequentially. To further clarify the interfacial interaction between $AgVO_3/V_2O_5$ and TiO_2, high-resolution XPS spectra of C 1s, Ti 2p, O 1s, V 2p, and Ag 3d in TiO_2 and $AgVO_3/V_2O_5$-TiO_2 hybrid were compared. For the C 1s spectrum of in TiO_2 and $AgVO_3/V_2O_5$-TiO_2, the peak at 284.8eV is assigned C = C, indicating that adding $AgVO_3$ and V_2O_5 does not introduce and change the C structure. The XPS data for TiO_2 and $AgVO_3/V_2O_5$-TiO_2 showed characteristic Ti $2p_{3/2}$ (458.48eV) and Ti$2p_{1/2}$ (464.57eV) peaks for Ti^{4+}, the binding energy at $AgVO_3/V_2O_5$-TiO_2 is reduced by about 0.22eV compared to the same peak of TiO_2 (Fig. 4(c)). This small shift may be due to the presence of additional V^{5+} and Ti^{3+} in $AgVO_3/V_2O_5$-TiO_2. The O 1s XPS spectra of both TiO_2 and $AgVO_3/V_2O_5$-TiO_2 in Fig. 4(d) show two typical peaks at ~ 530.2 and ~ 532.0 eV, which are attributed to lattice oxygen (Ti-O species) and a surface-adsorbed hydroxyl group (OH^-), respectively. As compared to TiO_2, it is clear that the O1s XPS spectrum of $AgVO_3/V_2O_5$-TiO_2 adds strong peaks (532.7eV) corresponding to the lattice oxygen (V-O or Ag-O). To gain insight into the oxidation state of V, we performed XPS characterization of all samples, as shown in Fig. 4e. The V 2p peak at 516.8(V^{4+}) ~ 517.6(V^{5+}) eV and 524.4eV are ascribed to the V $2p_{3/2}$ and V $2p_{1/2}$ levels, and the bare TiO_2 does not show any peaks of V, respectively [23–25]. As can be seen from Fig. 4(f), bare TiO_2 and V_2O_5-TiO_2 samples have no Ag peak position and Ag 3d peaks appear in $AgVO_3$-TiO_2 and $AgVO_3/V_2O_5$-TiO_2 samples, which is completely consistent with the experiment. From Fig. 4(f), it can be seen that the binding energies of 368.2eV and 374.2eV correspond to two distinct peaks of $3d_{5/2}$ and $3d_{3/2}$ for Ag 3d, respectively[21, 26]. Combining with the above XRD, SEM, TEM, and XPS maps, the above results prove.

3.2. UV-vis diffuse reflectance and bandgag mechanism

Efficient solar light absorption is vital factor for photoelectrocatalytic activity. Figure 5a displays bare TiO_2 absorbed light with an absorption onset at about 400nm, complying well with the theoretical bandgap (be calculated to 3.07eV) of rutile TiO_2[4, 27]. Figure 5(a) compares the UV–vis diffuse absorption spectra of the bare TiO_2, $AgVO_3$-TiO_2 V_2O_5-TiO_2 and $AgVO_3/V_2O_5$-TiO_2. Figure 5(a) and (b) show the composite photocatalysts can adjust the absorption cut-off wavelength. The visible light absorption intensity (VA) was estimated with VA (I×nm) of 7, 61, 144, 189 corresponds to the bare TiO_2, $AgVO_3$-TiO_2, V_2O_5-TiO_2 and $AgVO_3/V_2O_5$-TiO_2[4], respectively, as shown in Fig. 5(a). The prepared $AgVO_3/V_2O_5$-TiO_2 heterostructure has high light absorption properties in visible light (400nm ~ 700nm). Figure 5(b) shows the Tauc plot of UV-vis spectra, which reveals that the E_g of the bare TiO_2, $AgVO_3$-TiO_2, V_2O_5-TiO_2 and $AgVO_3/V_2O_5$-TiO_2 are about 3.07, 2.92, 2.12 and 1.41eV, respectively.

The reason for the high visible light absorption performance of the 1D $AgVO_3/V_2O_5$-TiO_2 heterostructures is described as follows. The conduction band, valence band and Fermi level of TiO_2, $AgVO_3$ and V_2O_5 are

shown in Fig. 5(c), it is shows the wide band gap of TiO_2 (~ 3.07eV) with coupling two band gaps small semiconductor materials V_2O_5 (~ 2.40eV) and $AgVO_3$ (~ 2.55eV) [4, 28, 29], but these three semiconductor materials are not premium heterojunctions if they cannot be synthesized into one material [6]. Fermi-level alignment refers to the fact that when semiconductor materials of different energy levels come into contact generally involves a redistribution of charge, which causes the shift in band edge positions [29, 30]. This indicates that when the heterostructure is formed, the Fermi energy of the $AgVO_3/V_2O_5$-TiO_2 semiconductor has to be the same. This leads to the CB and VB of both $AgVO_3$ and V_2O_5 to lie above TiO_2 as shown in Fig. 5(c). Specifically, when the sunlight shines on the surface of the $AgVO_3/V_2O_5$-TiO_2, since the CB of $AgVO_3$ and V_2O_5 are higher than bare TiO_2, a double type-II band alignment exists [6], and the photo-generated carriers are transferred from the CB of $AgVO_3$ and V_2O_5 to TiO_2. This double electron transfer paths can greatly enhance the separation of photogenerated electrons and holes. Similarly, the holes in the VB of TiO_2 transfer to the VB of $AgVO_3$ and V_2O_5 and facilitates the degradation of pollutants. Therefore, although the current configuration is not ideal for double type-II band gap heterojunctions, Efficient charge separation can still be achieved by Fermi-level alignment. This process can efficiently accelerate the separation of photo-induced e^-/h^+ pairs and prolong the e^-/h^+ pairs lifetime. The the double type-II band gap information is confirmed by the photocatalytic and the photoelectrochemical test results. This in turn can be used to elucidate the photocatalytic mechanism.

3.3 Photocatalytic property

Using the photocatalytic test evaluation described in Sect. 2.3, the photocatalytic degradation efficiency against Methylene blue under 150W simulated solar (AM 1.5G, 100mW/cm^2) irradiation. The absorption spectra decolorization curves of the MB solution after different photo-degradation time treatments with bare TiO_2 and $AgVO_3/V_2O_5$-TiO_2 are displayed in Fig. 6(a). After 120 min of simulated sunlight, the cannot be excited by visible light, so the MB degradation efficiency can only reach 49.9%, while the MB degradation rate of $AgVO_3/V_2O_5$-TiO_2 reached 95.8%. In Fig. 6(b) and (c), the photocatalytic performance of $AgVO_3/V_2O_5$-TiO_2 was outstanding, the photocatalytic degradation rates were 49.9%, 85.4%, 80.2%, 81.6%, and 95.8% for TiO_2, $AgVO_3$-TiO_2, V_2O_5-TiO_2, respectively.

According to kinetic principles, the recombination of photogenerated e^-/h^+ pairs can occur within 10^{-9}s to 10^{-12}s. When electron acceptors (pollutants) can be pre-sorbed on the catalyst surface, this is more favorable for photocatalytic performance. and the kinetics of the studied catalysts are shown in Fig. 6(d). The reaction rate constant of $AgVO_3/V_2O_5$-TiO_2 is 0.025min^{-1}, which is approximately five times that of TiO_2 (k = 0.005min^{-1}). The photocatalytic mechanism is shown in Fig. 5(c).The reaction rate constant order of the samples is as follows: TiO_2 < $AgVO_3$-TiO_2 < V_2O_5-TiO_2 < $AgVO_3/V_2O_5$-TiO_2. As mentioned above, the $AgVO_3$/ V_2O_5-TiO_2 sample demonstrated superior photocatalytic MB reduction activity compared to their sampls, with the main source of this superior activity is related to the reasonable heterojunction structure and the resultant photo-induced charge transfer properties.

3.4 Photoelectrochemical performance and water splitting

The photoelectrochemical (PEC) performances of the TiO_2, V_2O_5-TiO_2, $AgVO_3$-TiO_2 and $AgVO_3$/V_2O_5-TiO_2 nanorod arrays grown on FTO substrates were characterized. All the samples had been tested for 3h to investigate the stability. The separation, capture and migration of the photo-generated carriers on the surface of catalysts were investigated by Photocurrent, Electrochemical impedance spectroscopy (EIS) and Photoluminescence spectra (PL). Figure 7(a) shows a comparison of the current density responses of samples. For the bare TiO_2 (6μA), there was less photocurrent response due to its the intrinsic limitation of the quantum yield. The loads of $AgVO_3$-TiO_2 and V_2O_5-TiO_2 could further enhance the photocurrent response of TiO_2, while $AgVO_3$/V_2O_5-TiO_2 (115μA) presented higher response compared with $AgVO_3$-TiO_2 (15μA) and V_2O_5-TiO_2 (88μA). Importantly, $AgVO_3$/V_2O_5-TiO_2 exhibits the highest photocurrent, indicating a more efficient separation and longer lifetime of the charge carriers, which is in good accordance with the order of their photocatalytic measurements. The charge transfer characteristics of the photoelectrodes were further obtained by EIS analysis of different samples, and the results are presented in the form of Nyquist plots as shown in Fig. 7(b). The EIS response demonstrated the $AgVO_3$/V_2O_5-TiO_2 possessed a smaller impedance radius compared with TiO_2, $AgVO_3$-TiO_2 and V_2O_5-TiO_2, and creates a more suitable environment for holes transfer across the interface to the electrolyte [31]. The electron transport recombination properties was further confirmed by the results of PL. In Fig. 7(c), compared to TiO_2, the PL emission intensity of $AgVO_3$-TiO_2 and V_2O_5-TiO_2 and $AgVO_3$/V_2O_5-TiO_2 were dramatically decreased, and the $AgVO_3$/V_2O_5-TiO_2 shows the lowest intensity. The Nyquist plots and quenched PL intensity imply the effective charge transfer by the double type-II scheme heterojunction. Based on the PC, EIS, PL results, it provides strong support for the effective separation of e^-/h^+ pairs of $AgVO_3$/V_2O_5-TiO_2. It could be concluded that the two-step hydrothermal treatment has been shown to optimize the interface TiO_2 nanorod array, the reorganization rate of e^-/h^+ pairs was slowed down and the photocatalytic performance of PEC was significantly improved.

To evaluate the PEC performance of the TiO_2, $AgVO_3$-TiO_2, V_2O_5-TiO_2 and $AgVO_3$/V_2O_5-TiO_2, we performed linear sweep voltammogram (LSV) and Mott–Schottky (M-S) in an alkaline electrolyte. Figure 7(d) shows the photocurrent–potential (J–V) curves for the sample photoanodes under one standard simulated sunlight irradiation (100mW/cm^2). In Fig. 7(d), LSV curves of TiO_2, $AgVO_3$-TiO_2 and V_2O_5-TiO_2 and $AgVO_3$/V_2O_5-TiO_2 showed OER activity with initialpotentials of 1.93, 1.71, 1.64 and 1.47V to reach current density of 10mA/cm^2, respectively. Using the equation $\eta = E_{RHE} - 1.23$, the overpotential (η) of is calculated, as shown in Fig. 7(e). Clearly, the $AgVO_3$/V_2O_5-TiO_2 can serve as efficient OER electrocatalyst for practical application at high current density and exhibits the lowest onset overpotential (246.2mV), which is less than 446.9mV for bare TiO_2 (693.1mV). This enhancement can be attributed to the double type-II band gap of heterostructure. In addition, Fig. 7(f) shows indicates that the LSV curve of $AgVO_3$/V_2O_5-TiO_2 is lower (145.6mV) in the light source onset potential than in the dark, indicating a photocatalytic effect. Mott–Schottky (M-S) analysis has been proved to be an effective tool in studying

the electronic properties, by means of which can be determined flat band potentials (V_{FD}) and donor density (N_D) of samples. Here, the flat band potential of electrodes is determined by the Mott–Schottky equation [31–33]:

$$\frac{1}{C^2}=\left(\frac{2}{e_0 \varepsilon \varepsilon_0 N_D}\right)\left(V-V_{FB}-\frac{kT}{e_0}\right) \qquad \text{Equ. (1)}$$

$$N_D = \frac{2}{e\varepsilon\varepsilon_r}\left\{\frac{dE}{d\left(\frac{1}{C^2}\right)}\right\} \qquad \text{Equ. (2)}$$

with ε_0 (8.86×10^{-12}F/m) and ε (90F/m)-the passive oxide and vacuum permittivity, respectively; e-the electron charge (1.6×10^{-19}C); N_D-the donor density inside the passive oxide; V_{FB}-the flatband potential; *k*-the Boltzmann constant; T-the temperature (the value of kT/e_0 is 0.026V at 25°C). By extrapolation to $\frac{1}{C^2}=0$, the flat band potential V_{FB} can be determined. From Fig. 7(g), the slopes of Mott-Schottky plots show positive values for all samples, suggesting that the $AgVO_3$ QDs and V_2O_5 effect will not change the n-type conductivity of TiO_2. The V_{FB} of TiO_2, V_2O_5-TiO_2, $AgVO_3$-TiO_2 and $AgVO_3$/V_2O_5-TiO_2 derived from the extrapolation linear M-S plot to potential bias axis are 0.46V, 0.82, 1.06 and 1.27 versus RHE, respectively. As can be seen in Fig. 7(g), the slope of the Mott–Schottky plot for bare TiO_2 is much steeper than for the others amples. More specifically, According to Equ. (2), N_D values of the TiO_2, V_2O_5-TiO_2, $AgVO_3$-TiO_2 and $AgVO_3$/V_2O_5-TiO_2 photoelectrodes were calculated to be 4.3×10^{17}, 9.4×10^{17}, 6.4×10^{17} and 2.15×10^{18}cm^{-3}, respectively. After $AgVO_3$ and V_2O_5 modification, the N_D could be remarkably increased almost 5 times as compared with pristine TiO_2. This result reveals a drastic increase of free charge carriers in the $AgVO_3$ and V_2O_5 modified TiO_2 electrodes. To further confirm our deduction, the black and red lines show the fitting of the linear range of the Mott-Schottky plots for both in the dark and light $AgVO_3$/V_2O_5-TiO_2 based photoanodes. The fits shown in Fig. 7(h) yield V_{FB}=1.27V and $N_D=2.15\times10^{18}$cm^{-3} for in the light $AgVO_3$/V_2O_5-TiO_2 samples and V_{FB}=1.18V and $N_D=2.09\times10^{18}$cm^{-3} for in the dark $AgVO_3$/V_2O_5-TiO_2 samples, which shows that the increased quantity $\Delta N_D=6\times10^{16}$cm^{-3} derives from the effect of light and is consistent with the LSVcurve.

Conclusions

In summary, a high-flux double type-II scheme for interfacial electron transport channels was designed and synthesized using Fermi energy level realignment. In contrast to the bare TiO_2, V_2O_5-TiO_2 and $AgVO_3$-TiO_2, the $AgVO_3$/V_2O_5-TiO_2 heterojunction exhibited the best performance. The results indicated that a high-quality interfacial heterojunction contact is formed between V_2O_5 and $AgVO_3$ QDs using TiO_2 as a mediator, which can maximize the separation and transfer of photo-generated carriers. $AgVO_3$/V_2O_5-TiO_2 heterojunctions catalyst greatly enhanced the visible light absorption and improved the charge separation of TiO_2. It should be noticed that the enhanced light absorption may also play roles in photocurrent. The

$AgVO_3/V_2O_5$-TiO_2 was tested in Mott-Schottky and LSV performance with and without a light source, demonstrating that photoelectrochemical outperforms electrocatalysis. Highly ordered semiconductors show great prospects for applications in environmental photocatalysis and clean energy production, mainly due to their unique structures to realize efficient charge transport pathways and long-lived charges. This paper provides an innovative and stable $AgVO_3/V_2O_5$-TiO_2 double type-II band gap and p-n heterojunction for giant-internal electric field induced efficient photocatalysis and PEC overall water splitting.

Declarations

Conflicts of interest

The authors declare no competing financial interest.

Acknowledgements

This work was financially supported by National Natural Science Foundation of China

(No. 51772003, 51472003, 51701001, 61804039).

References

1. Cao S, Yan X, Kang Z, Liang Q, Liao X, Zhang Y (2016) **Band alignment engineering for improved performance and stability of $ZnFe_2O_4$ modified CdS/ZnO nanostructured photoanode for PEC water splitting**. Nano Energy 24:25–31
2. Wei Y, Kong J, Yang L, Ke L, Tan HR, Liu H, Huang Y, Sun XW, Lu X, Du H (2013) Polydopamine-assisted decoration of ZnO nanorods with Ag nanoparticles: an improved photoelectrochemical anode. J Mater Chem A 1(16):5045–5052
3. Nie Q, Yang L, Cao C, Zeng Y, Wang G, Wang C, Lin S (2017) Interface optimization of ZnO nanorod/CdS quantum dots heterostructure by a facile two-step low-temperature thermal treatment for improved photoelectrochemical water splitting. Chem Eng J 325:151–159
4. Yu H, Zhang M, Wang Y, Yang H, Liu Y, Yang L, He G, Sun Z: **A Facile and Controllable Vapor-Phase Hydrothermal Approach to Anionic S^{2-}-doped TiO_2 Nanorod Arrays with Enhanced Photoelectrochemical and Photocatalytic Activity**. *Nanomaterials (Basel)* 2020, 10(9)
5. Wang Y, Zhang M, Li J, Yang H, Gao J, He G, Sun Z (2019) **Construction of Ag@AgCl decorated TiO_2 nanorod array film with optimized photoelectrochemical and photocatalytic performance**. Appl Surf Sci 476:84–93
6. Marschall R (2014) Semiconductor Composites: Strategies for Enhancing Charge Carrier Separation to Improve Photocatalytic Activity. Adv Func Mater 24(17):2421–2440

7. Huang G, Mao J, Fan R, Yin Z, Wu X, Jie J, Kang Z, Shen M: **Integrated $MoSe_2$ with n + p-Si photocathodes for solar water splitting with high efficiency and stability**. *Applied Physics Letters* 2018, 112(1)
8. King LA, Zhao W, Chhowalla M, Riley DJ, Eda G: **Photoelectrochemical properties of chemically exfoliated MoS_2**. *Journal of Materials Chemistry A* 2013, 1(31)
9. Liu B, Sun Y, Wu Y, Liu K, Ye H, Li F, Zhang L, Jiang Y, Wang R (2020) Enhanced photoresponse of TiO2/MoS2 heterostructure phototransistors by the coupling of interface charge transfer and photogating. Nano Research 14(4):982–991
10. Zhou W, Shen B, Wang F, Zhang X, Zhao Z, Si M, Guo S (2020) **Enhanced photocatalytic degradation of xylene by blackening TiO_2 nanoparticles with high dispersion of CuO**. J Hazard Mater 391:121642
11. Shao M, Ning F, Wei M, Evans DG, Duan X (2014) Hierarchical Nanowire Arrays Based on ZnO Core – Layered Double Hydroxide Shell for Largely Enhanced Photoelectrochemical Water Splitting. Adv Func Mater 24(5):580–586
12. Chen X, Wang L, Li H, Cheng F, Chen J (2019) **Porous V_2O_5 nanofibers as cathode materials for rechargeable aqueous zinc-ion batteries**. Journal of Energy Chemistry 38:20–25
13. Hong Y, Jiang Y, Li C, Fan W, Yan X, Yan M, Shi W (2016) **In-situ synthesis of direct solid-state Z-scheme V_2O_5/g-C_3N_4 heterojunctions with enhanced visible light efficiency in photocatalytic degradation of pollutants**. Appl Catal B 180:663–673
14. Mondal M, Dutta H, Pradhan SK: **Enhanced photocatalysis performance of mechano-synthesized V_2O_5–TiO_2 nanocomposite for wastewater treatment: Correlation of structure with photocatalytic performance**. *Materials Chemistry and Physics* 2020, 248
15. Li S, Huang W, Xu H, Chen T, Ke Y, Qu Z, Yan N: **Alkali-induced deactivation mechanism of V_2O_5-WO_3/TiO_2 catalyst during selective catalytic reduction of NO by NH_3 in aluminum hydrate calcining flue gas**. *Applied Catalysis B: Environmental* 2020, 270
16. Zhang S, Zheng H, Sun Y, Li F, Li T, Liu X, Zhou Y, Chen W, Ju H (2020) **Oxygen vacancies enhanced photoelectrochemical aptasensing of 2, 3', 5, 5'-tetrachlorobiphenyl amplified with Ag_3VO_4 nanoparticle-TiO_2 nanotube array heterostructure**. Biosens Bioelectron 167:112477
17. Zhao W, Guo Y, Wang S, He H, Sun C, Yang S (2015) **A novel ternary plasmonic photocatalyst: ultrathin g-C_3N_4 nanosheet hybrided by Ag/$AgVO_3$ nanoribbons with enhanced visible-light photocatalytic performance**. Appl Catal B 165:335–343
18. Liu D, Chen D, Li N, Xu Q, Li H, He J, Lu J (2019) **Integration of 3D macroscopic graphene aerogel with 0D-2D $AgVO_3$-g-C_3N_4 heterojunction for highly efficient photocatalytic oxidation of nitric oxide**. Appl Catal B 243:576–584
19. Zhang X, Zhang J, Yu J, Zhang Y, Cui Z, Sun Y, Hou B (2018) **Fabrication of $InVO_4$/$AgVO_3$ heterojunctions with enhanced photocatalytic antifouling efficiency under visible-light**. Appl Catal B 220:57–66

20. Lin X, Guo X, Shi W, Guo F, Zhai H, Yan Y, Wang Q (2015) **Ag_3PO_4 quantum dots sensitized $AgVO_3$ nanowires: A novel $Ag_3PO_4/AgVO_3$ nanojunction with enhanced visible-light photocatalytic activity**. Catal Commun 66:67–72
21. Bavani T, Madhavan J, Prasad S, AlSalhi MS, AlJaafreh MJ (2021) **A straightforward synthesis of visible light driven $BiFeO_3/AgVO_3$ nanocomposites with improved photocatalytic activity**. Environ Pollut 269:116067
22. Liu Y, Guo W, Guo H, Ren X, Xu Q: **Cu (II)-doped V_2O_5 mediated persulfate activation for heterogeneous catalytic degradation of benzotriazole in aqueous solution**. *Separation and Purification Technology* 2020, 230
23. Silversmit G, Depla D, Poelman H, Marin GB, De Gryse R (2004) Determination of the V2p XPS binding energies for different vanadium oxidation states (V5 + to V0+). Journal of Electron Spectroscopy Related Phenomena 135(2–3):167–175
24. Zhang C, Wang J, Li Y, Li X, Koughia C, Wen S-J, Wong R, Yang Q, Kasap S (2019) **VO2 microrods synthesized from V_2O_5 thin films**. Appl Surf Sci 476:259–264
25. Yan C, Liu L: **Sn-doped V_2O_5 nanoparticles as catalyst for fast removal of ammonia in air via PEC and PEC-MFC**. *Chemical Engineering Journal* 2020, 392
26. Liu B, Han X, Mu L, Zhang J, Shi H (2019) **TiO_2 nanospheres/$AgVO_3$ quantum dots composite with enhanced visible light photocatalytic antibacterial activity**. Mater Lett 253:148–151
27. Liu X, Wu X, Xu T, Weng D, Si Z, Ran R (2016) **Effects of silica additive on the NH_3 -SCR activity and thermal stability of a V_2O_5/WO_3 -TiO_2 catalyst**. Chin J Catal 37(8):1340–1346
28. Wang Y, Su YR, Qiao L, Liu LX, Su Q, Zhu CQ, Liu XQ (2011) **Synthesis of one-dimensional TiO_2/V_2O_5 branched heterostructures and their visible light photocatalytic activity towards Rhodamine B**. Nanotechnology 22(22):225702
29. Gurulakshmi M, Selvaraj M, Selvamani A, Vijayan P, Sasi Rekha NR, Shanthi K (2012) **Enhanced visible-light photocatalytic activity of V_2O_5/S-TiO_2 nanocomposites**. Appl Catal A 449:31–46
30. Martha S, Das DP, Biswal N, Parida KM: **Facile synthesis of visible light responsive V_2O_5/N,S–TiO_2 composite photocatalyst: enhanced hydrogen production and phenol degradation**. *Journal of Materials Chemistry* 2012, 22(21)
31. Hong SJ, Lee S, Jang JS, Lee JS: **Heterojunction $BiVO_4/WO_3$ electrodes for enhanced photoactivity of water oxidation**. *Energy & Environmental Science* 2011, 4(5)
32. Hu W, Zheng M, Xu B, Wei Y, Zhu W, Li Q, Pang H (2021) Design of hollow carbon-based materials derived from metal–organic frameworks for electrocatalysis and electrochemical energy storage. Journal of Materials Chemistry A 9(7):3880–3917
33. Li D, Jia J, Zheng T, Cheng X, Yu X (2016) **Construction and characterization of visible light active Pd nano-crystallite decorated and C-N-S-co-doped TiO_2 nanosheet array photoelectrode for enhanced photocatalytic degradation of acetylsalicylic acid**. Appl Catal B 188:259–271

Figures

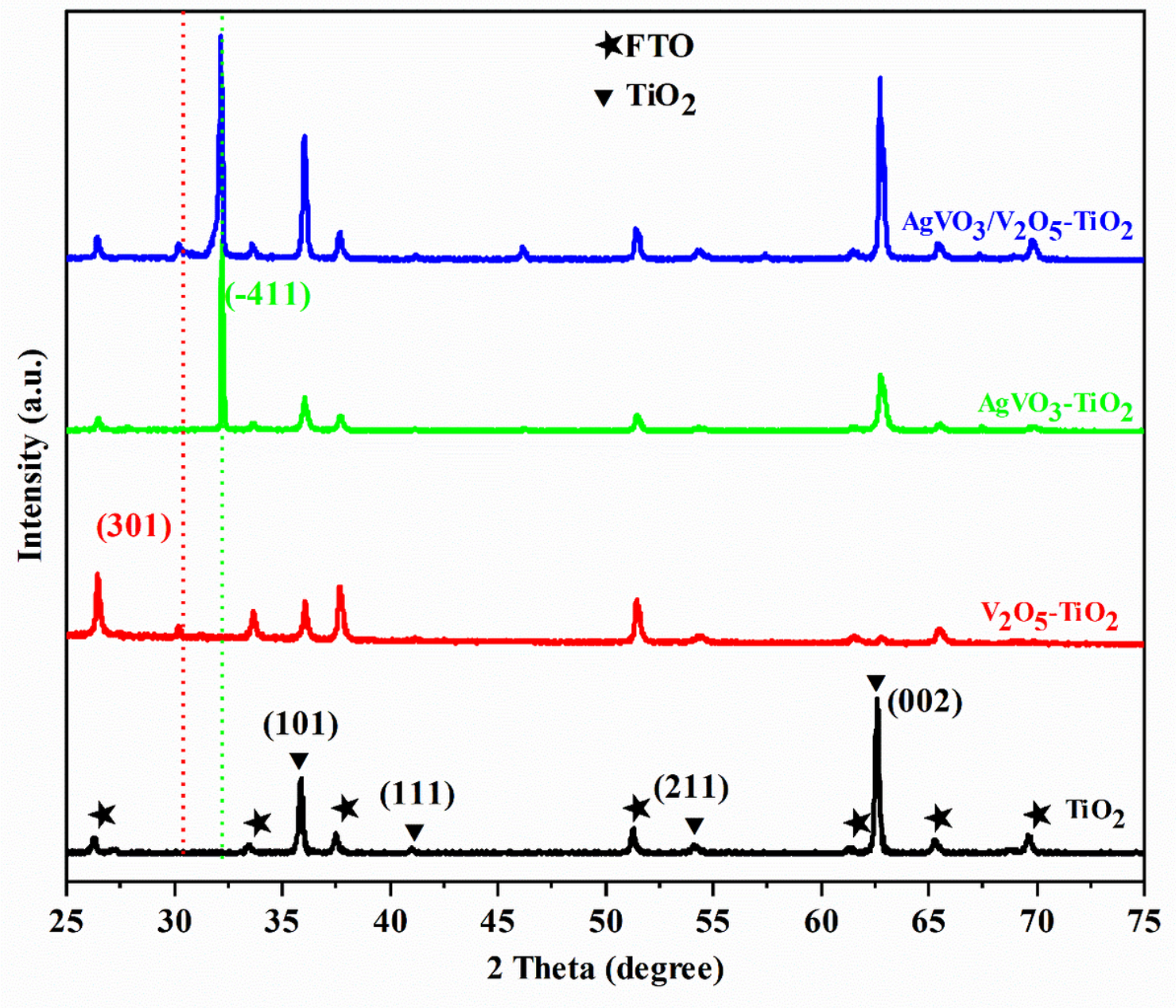

Figure 1

X-ray diffraction patterns of TiO2, V2O5- TiO2, AgVO3-TiO2 and AgVO3/V2O5-TiO2.

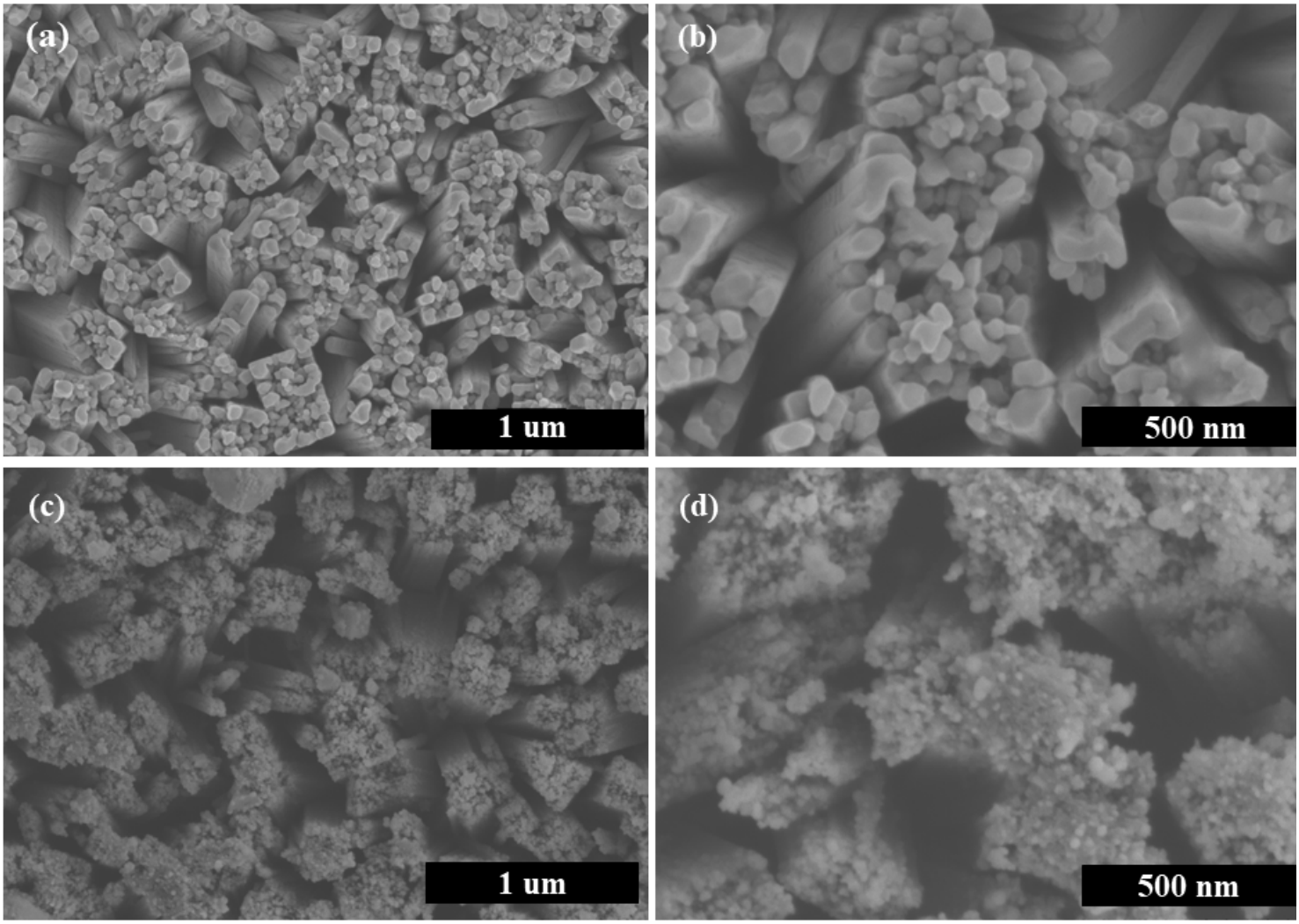

Figure 2

Top SEM images of the TiO2 and AgVO3/V2O5-TiO2. Scale bars (a and c) 1um, (b and d) 500nm.

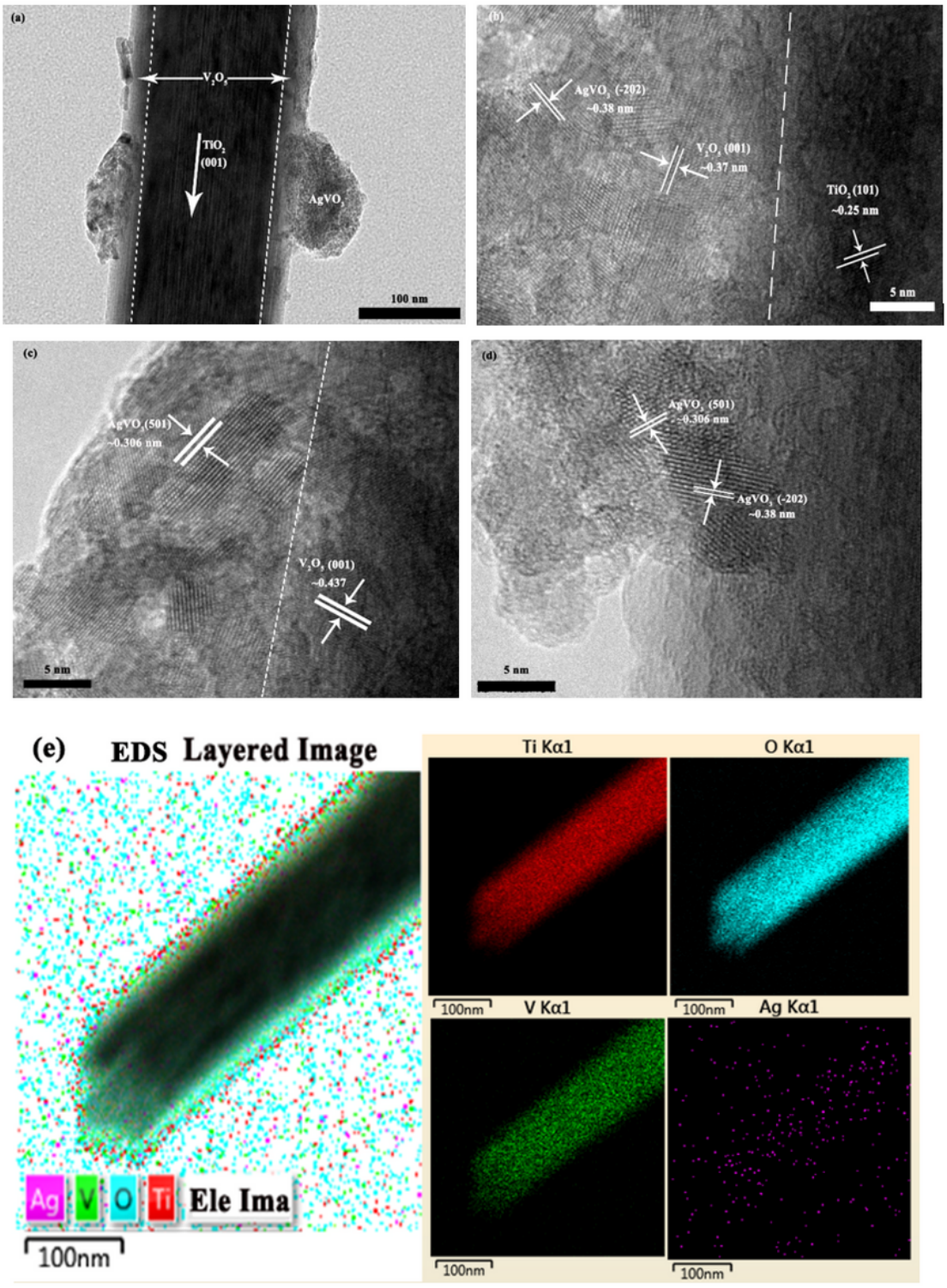

Figure 3

Microstructure characterization of AgVO3/V2O5-TiO2 NR. (a) Low-magnification TEM images. (b, c, d) High-resolution TEM images. (e) Elemental mapping of Ti, O, V, and Ag elements on AgVO3/V2O5-TiO2.

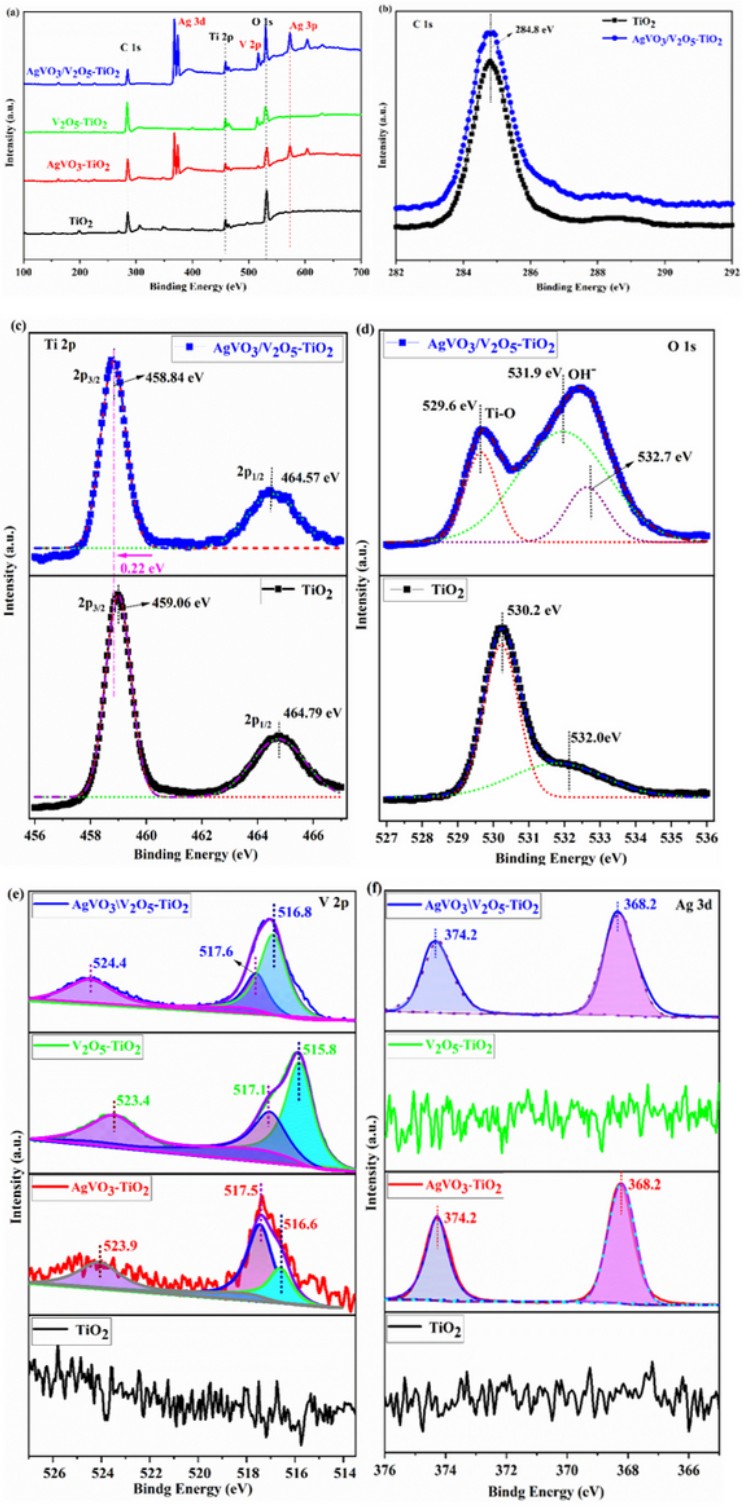

Figure 4

(a) XPS full spectrum. High-resolution XPS spectra of samples: (b) C 1s (c) Ti 2p (d) O 1s (e)V 2p (f) Ag 3d.

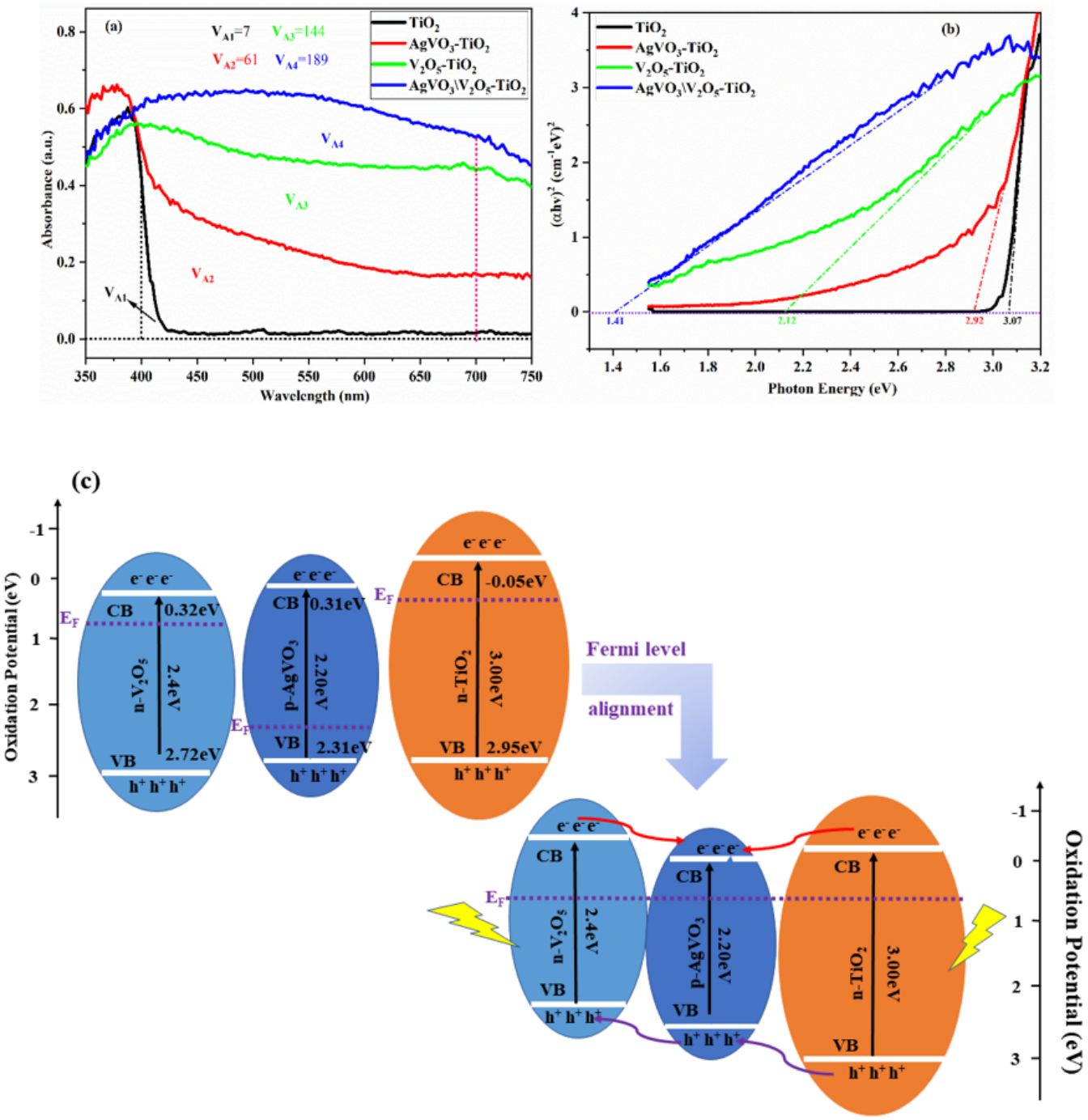

Figure 5

(a) UV–vis diffuse reflectance spectra of samples photoanodes. (b) Plots of (ahv)2 versus photon energy (hv) for the band gap energies of samples. (c) Schematic diagram of AgVO3/V2O5-TiO2 and charge separation of system under visible light.

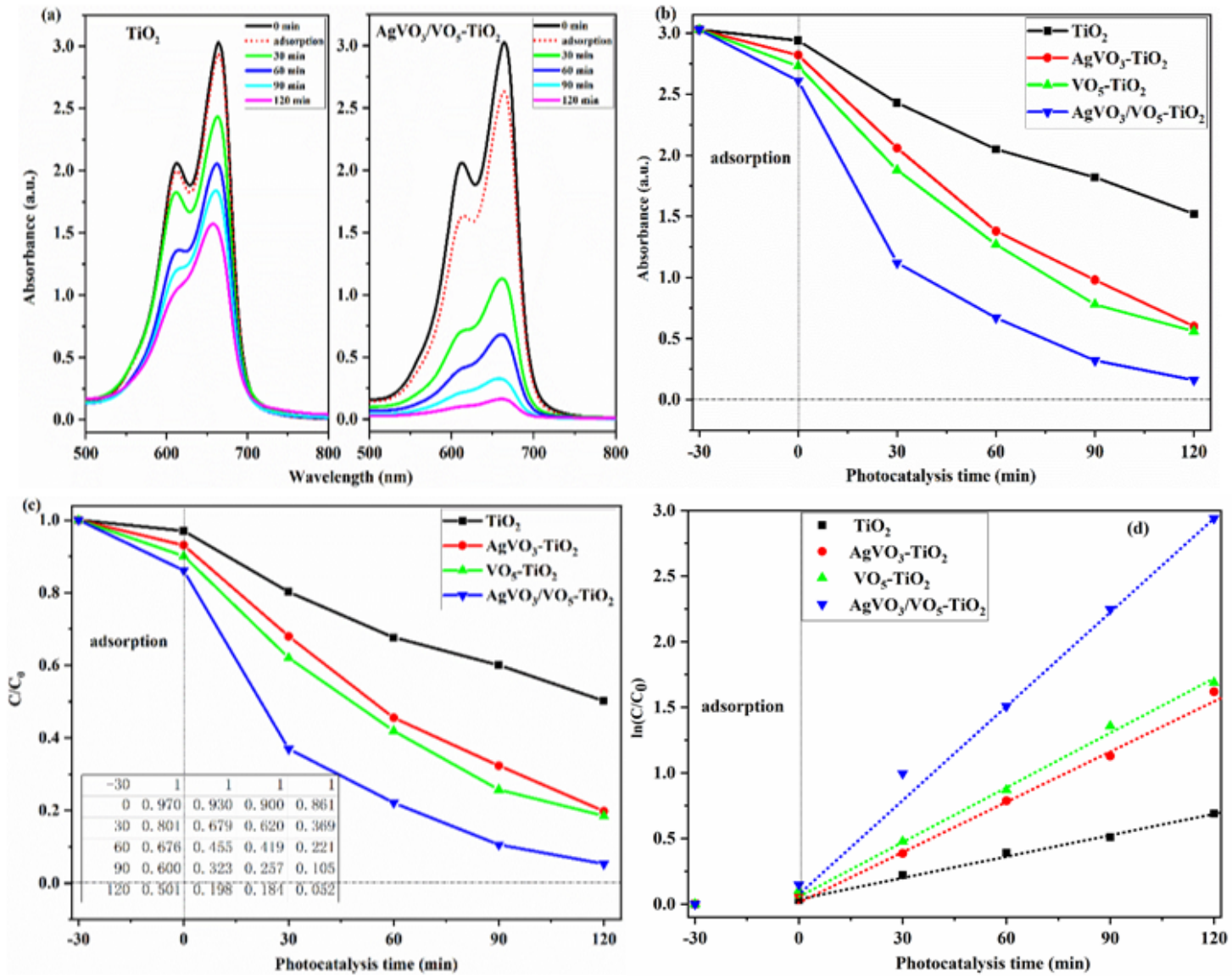

Figure 6

Photocatalytic activity for the degradation of Methylene blue: (a) UV-vis absorption spectrum of MB solution with 8gC/N/S-TiO2 and TiO2 under simulated solar light for various durations. (b) Photocatalytic degradation curves of MB by different samples. (c) corresponding kinetics and (d) rate constant (K) of MB degradation.

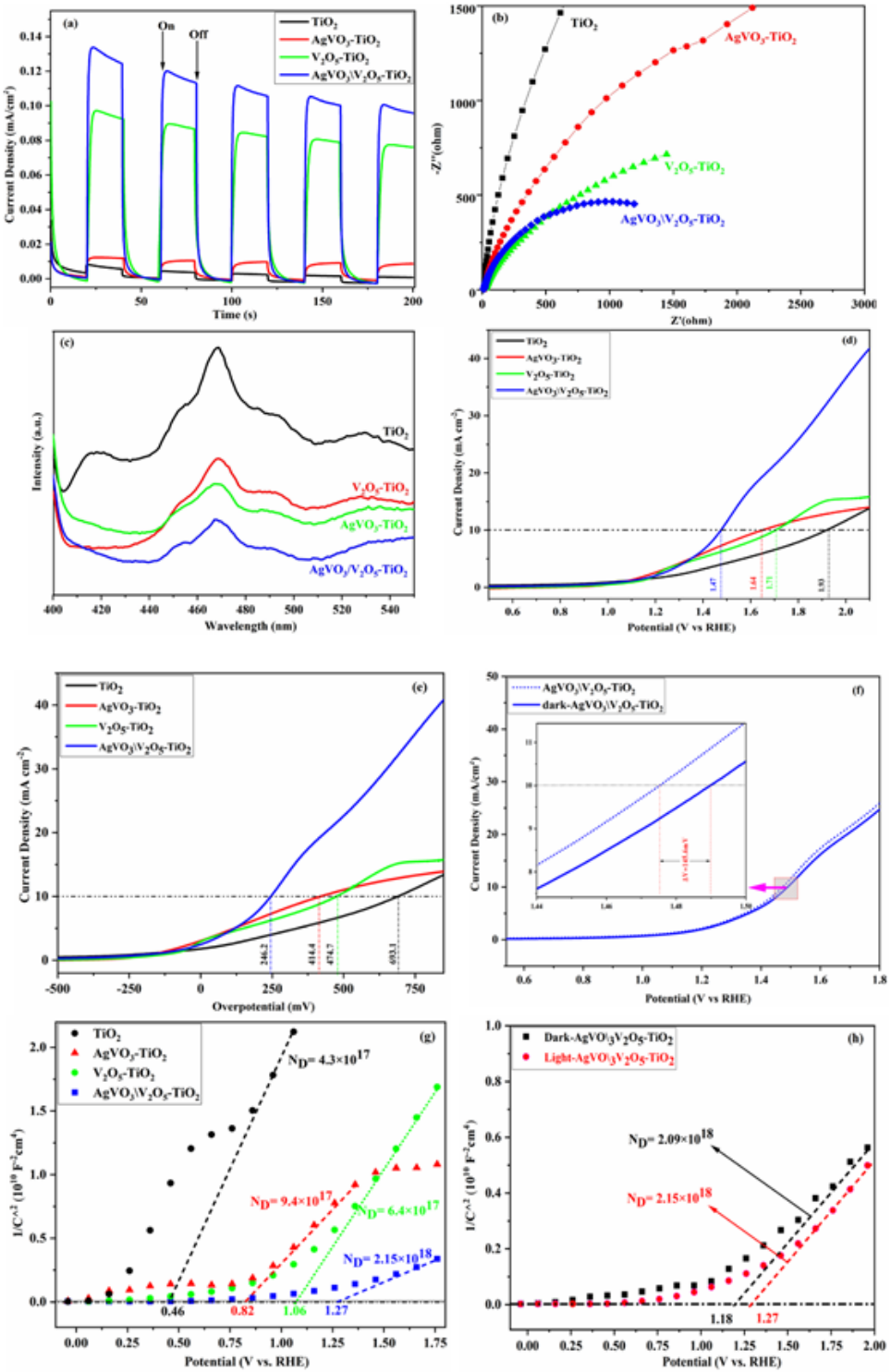

Figure 7

(a) Photocurrent responses for samples. (b) the impedance measurement of different samples. (c) The PL of different samples. (d, e, f) Hydrogen evolution reaction activities of samples. (g, h) Mott–Schottky plot of different samples.

Supplementary Files

This is a list of supplementary files associated with this preprint. Click to download.

- Scheme1.png